DSMC Modeling of Gasdynamics, Radiation and Fine Particulates in Ionian Volcanic Jets

J. Zhang, D. B. Goldstein, P. L. Varghese, N. E. Gimelshein, S. F. Gimelshein, D. A. Levin, and L. Trafton

Citation: AIP Conference Proceedings **663**, 704 (2003); doi: 10.1063/1.1581612

View online: http://dx.doi.org/10.1063/1.1581612

View Table of Contents: http://scitation.aip.org/content/aip/proceeding/aipcp/663?ver=pdfcov

Published by the AIP Publishing

DSMC Modeling of Gasdynamics, Radiation and Fine Particulates in Ionian Volcanic Jets

J. Zhang*, D.B. Goldstein*, P.L. Varghese*, N.E. Gimelshein†, S.F. Gimelshein†, D.A. Levin† and L. Trafton*

*The University of Texas at Austin, Austin, TX 78712
†Pennsylvania State University, University Park, PA 16802

INTRODUCTION

One of the most startling discoveries of the Voyager flybys of the moons of Jupiter was the existence of spectacular umbrella-like plumes over nine points on Io's surface [1]. Figure 1a shows a Galileo image of Io's surface and two such volcanic plumes. Many observations have been made of volcanic plumes on Io. Geissler *et al*. [2] examined the Galileo imaging of atmospheric emission from Io and tested the association of blue equatorial glows with specific volcanic plumes. Feldman *et al.* [3] showed the preferential absorption of Lyman-α emission by SO_2 at Io's equator in Hubble Space Telescope (HST) images and suggested that such a distribution could only arise from volcanic plume atmospheres. Strobel and Wolven [4] followed up on this idea and determined that only several volcanic plume sources near the equator are required to explain the HST observations. Most of the observations of planetary atmospheres, and all of those for Io, are via remote sensing of the radiation produced by, or transmitted through, the gas. Thus there is reason to develop advanced techniques to model, in an integrated way, the gas-dynamics of hypersonic volcanic jet flow along with its observable radiation signature. Some radiation features are associated with the fine particulates in the plumes. Photometric studies of one plume (Loki) by Collins [5] indicate that particles of various sizes (from 0.01 μm up to 1000 μm) are present. Strom and Schneider [1] suggested that the bright envelope appearing in the ultraviolet smoothed brightness images of Pele may be the result of a concentration of particles at a shock front. The wavelength dependence of the optical depth in 1996 HST observations of Pele can be matched by either a plume of SO_2 gas or a plume of very small scattering particles with maximum sizes of 0.08 μm. Thus, there is also reason to study the behavior of gas/particle flow in these volcanic plumes. Such techniques also have many other science and engineering applications [6, 7, 8, 9]. This paper describes the application of rarefied gas dynamics modeling techniques to understand radiation from and transport of particles in Ionian volcanic plumes.

Cook *et al*. [10] proposed ballistic and aerodynamic models to study the volcanic plumes on Io. Strom and Schneider [1] followed up on these models and obtained fits of the shape and brightness distribution of Prometheus. Ingersoll *et al*. [11] published a hydrodynamic model of the sublimation-driven flow of SO_2 gas. Ingersoll later [12] calculated the atmospheric response to volcanic sources by treating outflow from volcanic vents as a distributed source of mass (a line or point source). He investigated the effects of the patchy nature of the SO_2 frost and found that the only appreciable atmosphere on the dark side is in the vicinity of active volcanoes. Moreno *et al*. [13] used continuum computational fluid dynamics modeling of the volcanic plumes to characterize the nature of both the near-vent behavior as well as the spread of the down-falling gas over the planet. Lellouch [14] reported that Kieffer experienced numerical difficulties when modeling the underexpanded plumes on Io.

Rarefied gas dynamics modeling techniques developed for aerospace engineering applications are now quite sophisticated and have made it possible to study the complex dynamics of volcanic plume flow on Io in great detail. Some regions of the volcanic atmosphere resemble nozzle flow and hypersonic jets – typical aerospace engineering applications. The direct simulation Monte Carlo (DSMC) approach [15] pioneered by G. Bird is a suitable way to model the transitional to rarefied flows of these atmospheres and incorporate a wide range of detailed physics. Austin and Goldstein [16] presented preliminary results for DSMC models of Ionian plumes as early as 1995. They examined the nature of the shocks which develop in the plumes and how the plumes expand in the presence of a background non-

CP663, *Rarefied Gas Dynamics: 23rd International Symposium*, edited by A. D. Ketsdever and E. P. Muntz

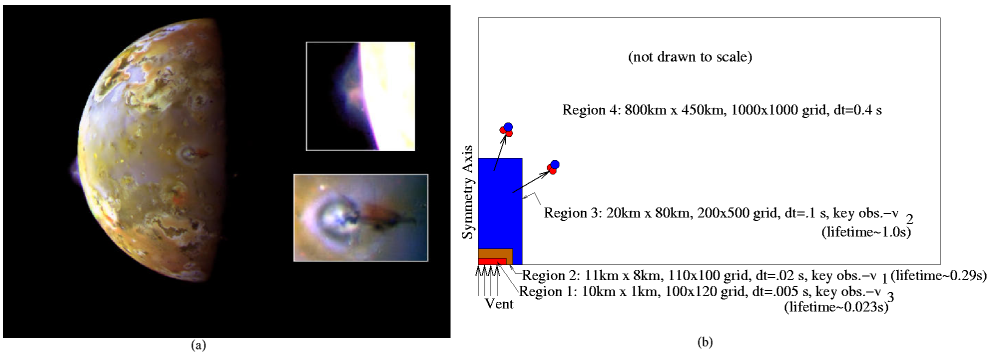

FIGURE 1. Io's volcanic plumes (a) and computational domain (b) used to model these plumes. In (a) Pillan Patera is seen on the limb while Prometheus is seen from above near the terminator (boundary between day and night).

condensible gas. Austin and Goldstein [17] also presented the first DSMC simulations of a sublimation/condensation driven circumplanetary flow as well as high spatial resolution modeling of a volcanic plume. A simple form of non-LTE infrared radiation from the SO_2 rotational states was incorporated. Austin and Goldstein [18] presented detailed calculations of sublimation/condensation driven flows including parametric studies of surface temperatures, the amount of non-condensible background gas, and energy input from the bombardment of the upper atmosphere by 57km/s sulfur and oxygen ions in Jupiter's co-rotating plasma torus [19]. The emphasis of [18] is on the atmospheric structure and the effect of different parameters on the observable frost deposition. We recently extended the previous work by Austin and Goldstein to examine the dynamics and radiation in volcanic plume flows in greater detail [20, 21]. There is also increasing recent interest in studying the transport of particles in a background fluid within DSMC method. Gallis *et al.* [8] applied such a technique to semiconductor manufacturing. Benson *et al.* [9] developed a model including particle (droplets) heating, desolvation, coalescence and transport.

Here, we briefly discuss a few example plume gasdynamics results along with the new results from gas/particle modeling in DSMC method.

MODEL

The volcanic flow is assumed to be axisymmetric and emerging at thermal equilibrium (vent temperature = 650 K, vent diameter based Knudsen number $\sim 10^{-4}$) and at a uniform velocity (1 km/s) from a circular vent centered at the origin of the symmetry axis. The height of the computational domain corresponds to the altitude above the surface of Io and the radius corresponds to the distance along the surface from the center of the vent. The gas is subject to Io's gravitational field after it erupts from the vent [16]. The molecules escape into space if they cross the upper boundary of the computational domain (rare) and are reflected by the outer specular wall when they collide with the circumferential boundary. The assumption of a specular wall at the outer boundary is not accurate. Yet we have shown that the outer wall is placed at a sufficient distance from the vent that it has no effect on the flow in the region of interest. The surface of Io is assumed to be very cold and rough and have a sticking coefficient of 1 so the molecules condense as they contact the surface. On the other hand, the surface sublimates vapor and the sublimation rate is specified by the equilibrium vapor pressure at the surface temperature [16]. Note that our sublimation/condensation model is greatly simplified by assuming sticking coefficient of 1 regardless of surface temperature. However, this assumption is probably quite realistic at surface temperature of less than 120 K [22]. Moreover, our sublimation/condensation boundary condition produces the correct equilibrium vapor pressure and a suitable gas outflux from the ice into a near-vacuum when the outflux should be independent of the influx.

The modeling of the IR radiation spectrum requires knowledge of the spatial distribution of the vibrational and rotational populations of SO_2. Translational-internal energy transfer as well as spontaneous emission processes must be modeled. During the gas dynamic computations, it is assumed that the densities are sufficiently low that the effects of absorption on the vibrational and rotational population may be ignored. This issue will be examined more closely in a future paper. On the other hand, absorption is accounted for when computing radiation spectra with GENSPECT [23].

The modeling of vibration-translation (VT) energy transfer during collisions between SO_2 molecules in DSMC is performed using a discrete version of the Larsen-Borgnakke method [24, 25]. A succession of redistributions, each of which involves only a single internal mode and the translational mode, can be used in the method. Since SO_2 molecules have three vibrational modes, advantage has been taken of this serial consideration of each mode in our DSMC model. The reason for treating the vibrational energy in a quantum fashion is that the vibrational levels are widely spaced and, at the relatively low temperatures of present interest, the vibrational modes can not be regarded as being fully excited.

Special effort has been placed on modeling the unique vibrational relaxation process of SO_2 molecules (discussed extensively in [26, 27, 28]). We assume $Z_{1,3}$=1000 for the V-T relaxation of the ν_1 and ν_3 modes: this $Z_{1,3}$ is expected to provide an acceptable accuracy for the temperatures of the order of several hundred Kelvins. In the temperature range of interest (100 - 650 K) the experimental data for Z_2 cluster around Z_2=300 and we use this constant value in the simulations. This simple assumption is justified because the uncertainty in the experimental relaxation data for Z_2 does not warrant a complicated curve fit, and the variation of Z_2 over this temperature range is small.

To model the radiation from vibrational bands, we need to know the probability for radiative transitions specified by the Einstein coefficient, A_{nm}, for the transition $n \rightarrow m$. This de-excitation probability for a molecule to undergo a spontaneous emission during the time step δt is found to be, $P = |(\delta n_1)_{1\rightarrow 0}/n_1| = 1.0 - e^{-A_{10}\delta t}$. For spontaneous IR cooling from the continuum of rotational states of SO_2, we retain the approach of Austin and Goldstein [17].

Numerical challenges arise when trying to include several mechanisms with very different time scales, the three vibrational band emissions in our case. Also, the plume flow experiences a wide range of flow regimes from the near-continuum regime to the free molecular regime. In the near-continuum regime, we need a very fine spatial and temporal resolution, while in the transitional and free molecular regimes we do not.

A multi-domain sequential calculation is used in our simulation. This approach is applicable because the flow is supersonic near the vent so it is not affected by downstream conditions. The whole domain is split into multiple subdomains and sequential calculations are performed from the inner to outer domains. Figure 1b shows a schematic diagram of this flowfield decomposition. The calculation parameters (domain size, grids, and timestep) and the key observables that drive their choice in each region are also shown in Fig. 1b. The flow field is first obtained for tiny region 1 with very fine spatial and temporal resolution to capture the signature of fast ν_3 band radiation. Molecules that cross the upper and right boundaries after steady state has been reached are stored as a source of input molecules for the calculation of region 2. During the calculation of the region 2, molecules are read in properly to give the correct number flux. The process of storing and re-reading molecules between concentric regions is carried on until the whole flow field has been obtained. In our case, four steps are necessary: three near the vent for radiation from the three vibrational bands, and one for the rest of the domain. An additional advantage of this sequential calculation is the good quality of the solution obtained near the vent where the vent diameter based Knudsen number ($\sim 10^{-4}$) is very low, while obviating the expense of carrying the very fine resolution through the whole domain.

The SO_2 vibrational spectra were computed from the flowfields calculated by DSMC as follows. First, number density and vibrational and translational temperatures were extracted along the axis of the plume. The data were also extracted along the 45° line that starts at the center of the vent. Then, these one-dimensional data were processed using the GENSPECT code [23]. GENSPECT is a line-by-line radiative transfer code to calculate gas absorption and emissivity, emission and transmission for a wide range of atmospheric gases from the near UV to the far IR. Given information including gas type, gas amount, temperature, pressure, path length and frequency range for an atmosphere or laboratory cell, the GENSPECT code computes the spectral characteristics of the gas. GENSPECT employs a new computation algorithm that maintains a specified accuracy for the calculation as a whole by pre-computing where a line function may be interpolated without a reduction in accuracy. The approach employs a binary division of the spectral range, and calculations are performed on a cascaded series of wavelength grids, each with approximately twice the spectral resolution of the previous one.

A line-by-line calculation implies that each line has two associated line-width parameters that describe the line shape at two extremes where the line-broadening behavior is well understood. One parameter describes behavior assuming only Lorentz broadening and one describes behavior assuming only Doppler broadening. Lorentz broadening tends to be the dominant effect at higher pressures while Doppler broadening is more significant at lower pressures (that occur in the conditions of interest). For temperatures and pressures of interest the actual line shape is a combination of the two effects, and a convolution of the two shapes, called the Voigt profile, is used in this work. The relative weighting of the convolution is controlled by additional parameters, along with pressure, partial pressure, and temperature [23].

Strom and Schneider [1] suggested that the bright envelope that appeared in the ultraviolet smoothed brightness images of Io's largest volcano, Pele, may be the result of a concentration of particles at a shock front. To see if this is a possible scenario, we studied the behavior of fine particulates in the volcanic plume. We tried two "overlay" methods to model the gas/particle flow. First, we treated the particles simply as another molecular species in DSMC.

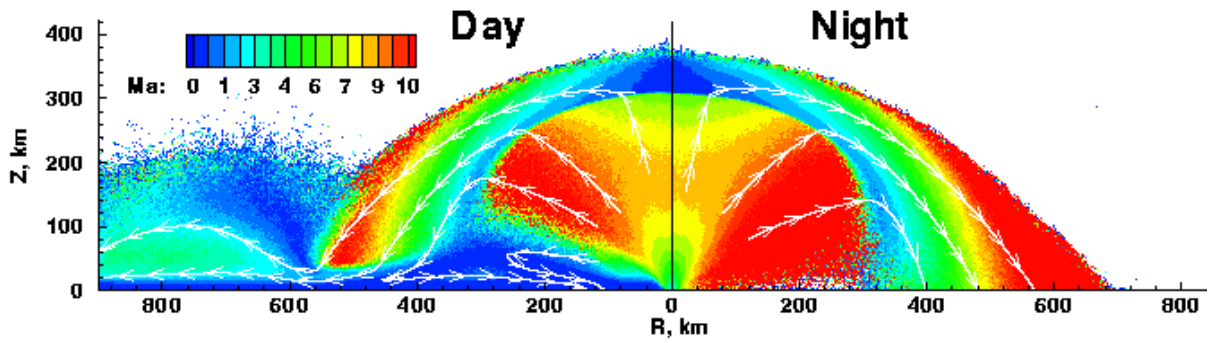

FIGURE 2. Comparison of Mach number contours with streamlines overlapped between dayside (left) with $T_{surface}$ = 115 K and nightside (right) Pele type plume with $T_{surface}$ = 90 K.

These "molecules" are huge in size compared to gas molecules and collide elastically with the gas molecules in a *pre-calculated* or frozen gas flowfield. The other is to calculate the drag on the particles in a pre-calculated gas flowfield and move the particles accordingly. In both methods, it is assumed that the fine particulates are spherical in shape, that the particle flow is so dilute that it has no effect on the gas flow, and the particles do not collide with each other. The mass density of the fine particulates is assumed to be 1.5×10^3 kg/m^3. Agreement between the results of both methods has been obtained, providing a measure of cross-validation. We focus on the second method at present mainly because of its efficiency and its capability of covering wide range of particle sizes. In this method, we also interpolate the pre-calculated gas flowfield to obtain a smooth particle flowfield, and use a predictor-corrector method to calculate the particle trajectories.

Photometric studies of Loki by Collins [5] indicate that the outer ultraviolet component consists of extremely fine particles (0.01–0.1 μm radius), while the inner component consists of larger particles (1–1000 μm). So the particle sizes we chose are in the range of 0.01–10 μm in diameter. The Knudsen number based on the diameter of the particle is of the order of 10^6 for 1 μm particles even at the volcano vent, so it is reasonable to assume collisionless flow to calculate the drag on the particle. Assuming cold particles, we use equation (7.71) obtained by Bird [15] for drag coefficient on a sphere in collisionless flow.

RESULTS

1. Gasdynamics and Radiation

Figure 2 shows a comparison of Mach number contours between a day-side and a night-side Pele type plume. It is seen that the flow fields look similar below and at the canopy shock: the gas erupts from the vent (centered at R = 0 km and about eight kilometers in radius) at around Mach 3, it expands, cools and accelerates until gravity slows it down and a canopy-shaped shock is formed at a height of about 300 km. The flows look quite different as the gas that crosses the canopy shock falls to the ground. A re-entry shock is formed in the day-side plume as a result of the interaction between the falling gas and the ground frost sublimation atmosphere. Such a shock is not seen in the night-side plume since the background atmosphere is negligible and all plume particles reach the condensing surface. The plotted streamlines show that for the day-side Pele type plume the sublimation atmosphere is dense enough to split the falling gas into two parts: one part is reflected up and turned further away from the vent, the other part is turned inward.

A parametric study is carried out to further examine the nature of the impingement of the falling hypersonic gas onto a sublimating surface. Several different surface temperatures around 108 K were examined and three such flowfields are compared in Fig. 3. It is found that the interaction between the impinging hypersonic gas and the atmosphere is quite sensitive to the surface temperature, and the flow structure around the interacting region changes dramatically even for a small change in the surface temperature (105 to 111 K). At a surface temperature of 105 K, the sublimation atmosphere is not dense enough to decelerate and turn the falling gas so that most of the falling molecules are simply pouring onto the ground and condense unimpeded.

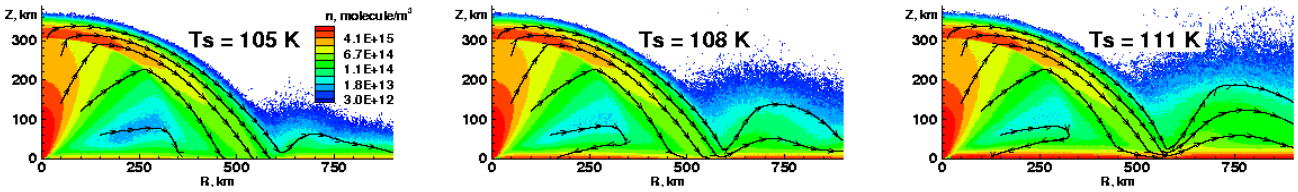

FIGURE 3. Number density contours of the flowfields with different surface temperatures. Notice the formation of a well defined bounce region at higher temperature.

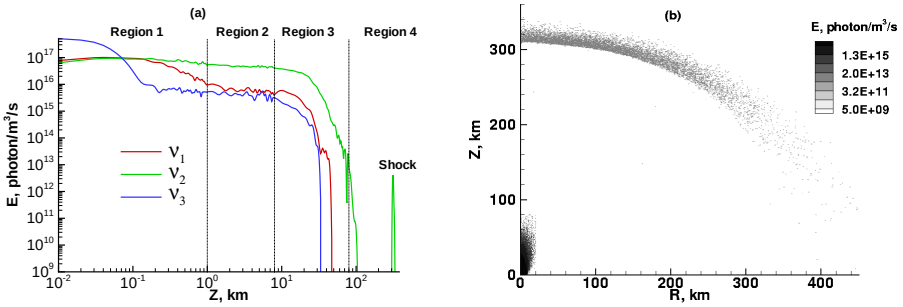

FIGURE 4. (a) Profiles of photon emission rate (photon/m^3/s) of ν_1 (1151 cm^{-1}), ν_2 (518 cm^{-1}) and ν_3 (1362 cm^{-1}) vibrational bands of SO_2 along the symmetry axis. Also shown are the locations of each subdomain. (b) Contours of photon emission rate for the ν_2 (518 cm^{-1}) band for the whole flow field for nightside Pele type plume.

The amount of the falling gas that is decelerated and turned becomes larger as the surface temperature rises and the sublimation atmosphere becomes more dense. Most of the gas is either turned inwards or outwards and the re-entry shock is clearly formed at a surface temperature of 111 K. This surface temperature of 111 K is interpreted as the critical temperature, at which the sublimation atmosphere surface vapor pressure is just high enough to balance the stagnation pressure behind a nearly horizontal re-entry shock. This interpretation was confirmed by a similar parametric study performed for a plume of ten times lower vent number density, in which case the critical surface temperature defined above is first estimated to be 104 K, and the prediction works quite well. (It is also found that the ten times lower vent number density plume retains more translational energy to rise higher and expand wider due to the lack of inter-molecular collisions and radiation losses.)

The resulting surface deposition patterns also change dramatically. At low surface temperatures, the falling gas simply pours onto the surface and condensation dominates to build up a deposition ring at R = $\sim$ 500 km. As the surface temperature increases, the SO_2 frost begins to be depleted at the onset of the turning of the impinging flow. We believe that both the outward and inward turning flows entrain the upper part of the sublimation atmosphere which results, surprisingly, in a slightly lower surface pressure than the equilibrium vapor pressure; this causes the depletion of SO_2 frost from the surface by sublimation.

Figure 4a shows profiles of photon emission rate in the three vibrational bands of SO_2 along the symmetry axis. Figure 4b provides contours of photon emission rate for the ν_2 (518 cm^{-1}) band for the whole flow field. It is seen that ν_1 and ν_3 band emissions start at $\sim 10^{17}$ photon/m^3/s and drop to $\sim 10^{16}$ photon/m^3/s within 2 km. These rapid emissions are captured by the calculation in region 1 and 2 with very fine spatial and temporal resolution. A balance between emission and collisional excitation is established beyond Z = $\sim$2 km for these two bands, so the emission rate stays relatively constant until the gas density drops so low that the balance is broken in region 3. The emission in the ν_2 band is relatively slow (A_{10} = 0.88 s^{-1}) and collisional excitation keeps the emission rate relatively constant up to region 3. At higher altitude, the vibrational energy of the gas is not strongly replenished from translational energy through inter-molecular collisions, since the gas density and thus the collision excitation rate is low. Taking the ν_3 band for example, the radiative lifetime of the ν_3 vibrational state is $\sim$23 ms but the collision relaxation time for ν_3 vibrational-translational energy transfer at an altitude of $\sim$30 km is $\sim$20 s. The gas is thus in a highly non-equilibrium state and the vibrational temperatures for the three vibrational modes become very low by an altitude of $\sim$50 km, $\sim$35 km, and $\sim$30 km, for ν_2, ν_1 and ν_3 bands, respectively.

When the flow reaches the canopy shock, it is again compressed and heated. The inter-molecular collisions become

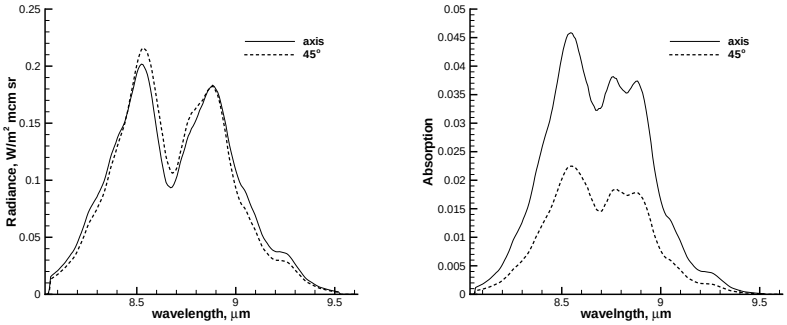

FIGURE 5. IR radiance (a) and absorption (b) spectra for the ν_1 band for a night-side Pele-type plume.

sufficiently frequent that the ν_2 mode is re-excited and emission from the ν_2 band re-appears at the shock. However, emission in the other two bands does not reappear. This is because the collision relaxation time at the shock for ν_1 and ν_3 vibrational-translational energy transfer is relatively long ($\sim$100 s) and the inter-molecular collisions are not sufficiently frequent to maintain any appreciable emission.

We next consider the spectra for different infrared bands of SO_2 that originate from the de-excitation of different vibrational modes. Figures 5a and 5b show IR spectra for the ν_1 band for a night-side Pele-type plume. Here, spectral resolution was 10^{-4} μm. The vibrational temperature of the first vibrational band in the DSMC computations was essentially 0 for altitudes higher than 35 km (the DSMC computations did not include absorption). That means that the molecules are primarily in the ground vibrational states at those altitudes, ν_1 emission does not occur at high altitudes, and absorption is the only process that affects the spectra. However, the low number density at high altitudes causes the plume to be nearly transparent (see Fig. 5b that shows the fraction of radiance absorbed), meaning that nearly all emission generated by the lower, heated layers makes its way to the top unabsorbed. The total emission for the viewing angle of 0° (parallel to the vent axis) can be estimated to be $7.5 \cdot 10^6$ W/sr. As the figure shows, the radiation intensity depends only slightly on the viewing geometry, as spectra along a 45° line to the symmetry axis are only slightly different in magnitude from that for a 0° line. Similarly, the total emission for 45° viewing angle can be estimated to be approximately the same as for 0°.

2. Fine Particulates

Figure 6 shows the shapes of the gas and particle jets. The gas density contours and the particle locations are plotted, the latter represented by small dots. Note that the particles are simply placed in the flow at the vent orifice at zero velocity and the gas flow drags them upward. Several interesting features appear as the particle size increases. The first remarkable feature is that a concentration of particles at or near the canopy shock clearly appears for d = 0.01 μm particles. Further calculations show that such accumulation occurs for particles up to 0.1 μm (though below the shock). These results provide strong support to Strom and Schneider's suggestion as to the cause of the bright envelope appearing in the ultraviolet smoothed brightness images of Pele and also agree with the size range of the outer ultraviolet component found by Collins [5]. Also interesting is the relatively distinct underside of the outer portion of the particulate canopy (labeled A). This feature will be explained in the discussion of Fig. 7. In the three parts of Fig. 6 one can see the large differences in particle deposition patterns for different particle sizes. For smaller sizes ($\sim$0.01 μm), the motion of the particles is strongly coupled with that of the gas so the range of deposition of falling particles is relatively narrow and within the band where the gas condenses. As the particle size increases, the particle deposition band is broadened and moves inward. Larger particles ($\sim$1 μm) do not follow the gas well and their motions are much less influenced by the gas once they leave the near-vent region. They do not reach the canopy shock (as the smaller particles do) and they fall close to the vent. No other notable features appear for particles with a size larger than 1 μm except that the larger the particles, the lower they rise and the closer to the vent they land. The largest particles that could be entrained in our simulated plume are found to be $\sim$30 μm. This was determined by equating drag to weight, where weight = mg and drag = $C_d \frac{1}{2} \rho u_v^2 \sigma$. Here, m is the mass of particle, g is the gravitational

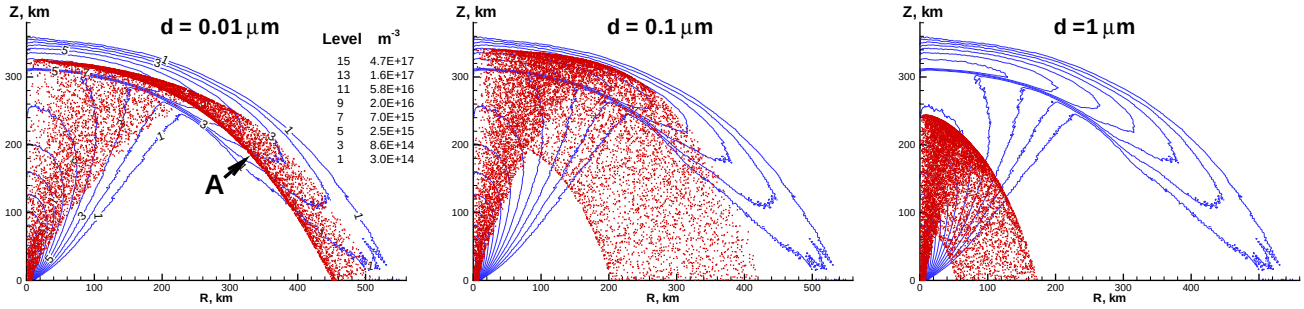

FIGURE 6. Shape of the gas and particle jets for different particle sizes (d = 0.01, 0.1 and 1 μm). Note that particle locations are represented by small dots.

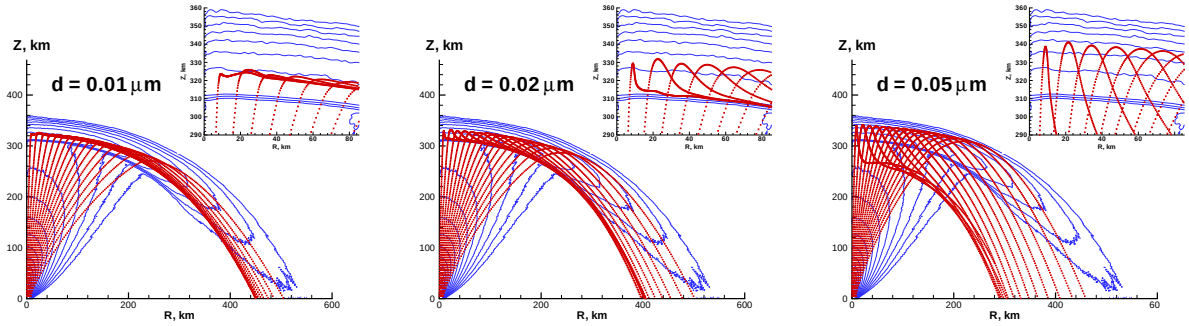

FIGURE 7. Trajectory (small dots) of different size particle (d = 0.01, 0.02 and 0.05 μm) with insets showing the vicinity of the canopy shock near the symmetry axis. Also shown are the same gas density contours as in Fig. 6.

acceleration, C_d is the drag coefficient obtained by using equation (7.71) by Bird [15], ρ and u_v are the gas density and the freestream velocity at the vent, and σ is the cross-sectional area of particle.

To examine how the above features are formed, we ran a parametric study on the trajectories of particles with sizes between 0.01 and 0.05 μm. Figure 7 shows those trajectories and the gas density contours. Insets showing the vicinity of the canopy shock are also plotted. The motions of the particles show few differences before they reach the canopy shock: they all reach and cross the shock, and are slowed down by the shock. This slowing down in the motions of particles results in the concentration of particles near the shock. Particles in the size range 0.01–0.02 μm cross the shock, reach a maximum altitude, and then begin to fall under the action of gravity. The falling particles are dragged outward by the gas shear flow created between the rising and falling gas and the particle trajectories tend to cluster along density iso-contours, and this creates a distinct underside to the particle canopy (labeled A in Fig. 6). As might be expected the larger particle trajectories cluster at lower altitudes closer to the canopy shock. Larger particles (0.05 μm) have somewhat different trajectories. Because of their inertia, they are not slowed down as much by the shock, and so reach *higher* maximum elevations, before falling back towards the surface. The drag of the flow on these falling particles turns them outwards but they re-cross the shock, before the trajectories are clustered by the upcoming supersonic gas. The envelope of the radial deflection again forms a relatively distinct underside of particle canopy but below the shock.

In reality, a wide range of particle sizes is expected in the plume, so a distinct particle canopy would not be observed. However, the calculations indicate that there will be a sorting of the particles by size away from the vent and on the surface, with finer particles falling further away. Large particles stay close to the plume axis and form a dense column. Scattering from these particles may be the reason why one sees a bright column in sunlight in many Galileo plume images. However, this does not mean that the gas plume stays only in a column and does not expand much, so one should be careful and specific when interpreting the shape of the plume based on these images.

Finally, note the wave-like motion in those particle (0.01 and 0.02 μm) trajectories that are close to the symmetry axis above the shock. We suggest that these waves are caused by the vertical oscillation of particles inside a non-

uniform gas flow (either having a density or velocity gradient or both) around an equilibrium height under the action of gravity and the drag by the gas. The frequency of this oscillation is:

$$\sqrt{\frac{-C_d \frac{1}{2}\sigma(2\rho u_v \frac{du_v}{dz} + {u_v}^2 \frac{d\rho}{dz})}{m}} \tag{1}$$

which was observed in our simulations.

ACKNOWLEDGMENTS

This research was based in part on and developed from previous work by J. V. Austin and D. B. Goldstein. The work at the University of Texas at Austin was supported by the NASA Planetary Atmospheres Program, Grant No. NASA NAG5-8143. We would also like to acknowledge support for the work performed at George Washington University and at Pennsylvania State University to Grant No. NASA NAG5-8068. We also thank K. Retherford at Johns Hopkins University for his helpful comments.

REFERENCES

1. Strom, R. G., and Schneider, N. M., *Satellites of Jupiter*, Univ. of Arizona Press, Tucson, 1982, pp. 598–633.
2. Geissler, P. E., McEwen, A. S., lp, W., Belton, M. J. S., Johnson, T. V., Smyth, W. H., and Ingersoll, A. P., *Science*, **285**, 870–874 (1999).
3. Feldman, P. D., Strobel, D. F., Moos, H. W., Retherford, K. D., Wolven, B. C., McGrath, M. A., Roesler, F. L., Woodward, R. C., Oliverson, R. J., and Ballester, G. L., *Geophys. Res. Lett.*, **27**, 1787–1790 (2000).
4. Strobel, D. F., and Wolven, B. C., *Astrophys. Space Sci.*, **277**, 271–287 (2001).
5. Collins, S. A., *J. Geophys. Res.*, **86**, 8621–8626 (1981).
6. Rijov, Y. A., Svirschevsky, S. B., and Kuzovkin, K. N., "VEGA Spacecraft Aerodynamics in the Gas-Dust Rarefied Atmosphere of Halley's Comet," in *Rarefied Gas Dynamics: Physical Phenomena*, edited by E. P. Muntz, D. P. Weaver, and D. H. Campbell, AIAA, Washinton DC, 1988, pp. 23–39.
7. Combi, M. R., Kabin, K., DeZeeuw, D. L., Gombosi, T. I., and Powell, K. G., *Earth, Moon, and Planets*, **79**, 275–306 (1997).
8. Gallis, M. A., Rader, D. J., and Torczynski, J. R., *AIAA 2002-2760* (2002).
9. Benson, C. M., Zhong, J., Gimelshein, S. F., Levin, D. A., and Montaser, A., *AIAA 2002-3183* (2002).
10. Cook, A. F., Shoemaker, E. M., and Smith, B. A., *Nature*, **280**, 743–746 (1979).
11. Ingersoll, A., Summers, M. E., and Schlipf, S. G., *Icarus*, **64**, 375–390 (1985).
12. Ingersoll, A., *Icarus*, **81**, 298–313 (1989).
13. Moreno, M. A., Schubert, G., Baumgardner, J., Kivelson, M. G., and Paige, D. A., *Icarus*, **93**, 63–81 (1991).
14. Lelloch, E., *Icarus*, **124**, 1–21 (1996).
15. Bird, G., *Molecular Gas Dynamics and Direct Simulation of Gas Flows*, Clarendon Press, Oxford, 1994, ISBN 0-19-856195-4.
16. Austin, J., and Goldstein, D., *Molecular Physics and Hypersonic Flows*, Kluwer Academic Publishers, Netherlands, 1995, pp. 749–758.
17. Austin, J., and Goldstein, D., "Direct Numerical Simulation of Supersonic Rarefied Atmospheric Flows on Io," in *Rarefied Gas Dynamics: Proceedings of the 21st International Symposium on Rarefied Gas Dynamics*, edited by R. Brun, R. Campargue, R. Gatignol, and J. C. Lengrand, Cépaduès Éditions, Marseille, France, 1998.
18. Austin, J., and Goldstein, D., *Icarus*, **148**, 370–383 (2000).
19. Spencer, J., and Schneider, N., *Annu. Rev. Earth Planet. Sci.*, **24**, 125–190 (1996).
20. Zhang, J., Goldstein, D. B., Gimelshein, N., Gimelshein, S., Levin, D., and Varghese, P., *AIAA paper 2001-2767* (2001).
21. Zhang, J., Goldstein, D. B., Varghese, P., Gimelshein, N., Gimelshein, S., and Levin, D., *Submitted to Icarus* (2002).
22. Sandford, S. A., and Allamandola, L. J., *Icarus*, **106**, 478–488 (1993).
23. Quine, B. M., and Drummond, J. R., *The Journal of Quantitative Spectroscopy and Radiative Transfer*, **74** (2000).
24. Larsen, P., and Borgnakke, C., "Paper A4," in *Rarefied Gas Dynamics*, edited by M. Becker and M. Fiebig, CFVLR, Porz-Wahn, Germany, 1974.
25. Bergemann, F., and Boyd, I. D., "DSMC simulation of inelastic collisions using the Borgnakke-Larsen method extended to discrete distributions of vibrational energy," in *Rarefied Gas Dynamics: Theory and Simulations*, edited by B. D. Shizgal and D. P. Weaver, Progress in Astronautics and Aeronautics, 1994, pp. 174–183.
26. Lambert, J., and Salter, R., *Proc. Roy. Soc.*, **243**, 78–83 (1957).
27. Bass, H. E., Winter, T. G., and Evans, L. B., *J. Chem. Phys.*, **54**, 644 (1971).
28. Lambert, J. D., *Vibrational and Rotational Relaxation in Gases*, Oxford University Press, Oxford, 1977.